Journal of Marine Science and Technology

Volume 25 | Issue 5 Article 12

INTENSIFICATION AND DECAY OF TYPHOON NURI (2014) ASSOCIATED WITH COLD FRONT AND SOUTHWESTERLY AIRFLOW OBSERVED IN SATELLITE CLOUD IMAGES

Kuan-Dih Yeh
Dept. of Electrical Engineering, Chien Hsin University of Science and Technology, Chung-li, Tao-yuan, Taiwan, R.O.C., kdyeh@uch.edu.tw

Ji-Chyun Liu
Dept. of Electrical Engineering, Chien Hsin University of Science and Technology, Chung-li, Tao-yuan, Taiwan, R.O.C.

Chee-Ming Eea
Dept. of Electrical Engineering, Chien Hsin University of Science and Technology, Chung-li, Tao-yuan, Taiwan, R.O.C.

Ching-Huei Lin
Dept. of Electrical Engineering, Chien Hsin University of Science and Technology, Chung-li, Tao-yuan, Taiwan, R.O.C.

Wen-Lung Lu
Dept. of Electrical Engineering, Chien Hsin University of Science and Technology, Chung-li, Tao-yuan, Taiwan, R.O.C.

See next page for additional authors

Follow this and additional works at: https://jmstt.ntou.edu.tw/journal

Recommended Citation

Yeh, Kuan-Dih; Liu, Ji-Chyun; Eea, Chee-Ming; Lin, Ching-Huei; Lu, Wen-Lung; Chiang, Ching-Tsan; Lee, Yung-Sheng; and Chen, Ada Hui-Chuan (2017) "INTENSIFICATION AND DECAY OF TYPHOON NURI (2014) ASSOCIATED WITH COLD FRONT AND SOUTHWESTERLY AIRFLOW OBSERVED IN SATELLITE CLOUD IMAGES," *Journal of Marine Science and Technology*: Vol. 25: Iss. 5, Article 12.
DOI: 10.6119/JMST-017-0706-1
Available at: https://jmstt.ntou.edu.tw/journal/vol25/iss5/12

This Research Article is brought to you for free and open access by Journal of Marine Science and Technology. It has been accepted for inclusion in Journal of Marine Science and Technology by an authorized editor of Journal of Marine Science and Technology.

INTENSIFICATION AND DECAY OF TYPHOON NURI (2014) ASSOCIATED WITH COLD FRONT AND SOUTHWESTERLY AIRFLOW OBSERVED IN SATELLITE CLOUD IMAGES

Acknowledgements

We gratefully acknowledge Professor Liou Y. A. of the Center for Space and Remote Sensing Research at National Central University, Taiwan.

Authors

Kuan-Dih Yeh, Ji-Chyun Liu, Chee-Ming Eea, Ching-Huei Lin, Wen-Lung Lu, Ching-Tsan Chiang, Yung-Sheng Lee, and Ada Hui-Chuan Chen

This research article is available in Journal of Marine Science and Technology: https://jmstt.ntou.edu.tw/journal/vol25/iss5/12

Journal of Marine Science and Technology, Vol. 25, No. 5, pp. 599-606 (2017)
DOI: 10.6119/JMST-017-0706-1

INTENSIFICATION AND DECAY OF TYPHOON NURI (2014) ASSOCIATED WITH COLD FRONT AND SOUTHWESTERLY AIRFLOW OBSERVED IN SATELLITE CLOUD IMAGES

Kuan-Dih Yeh[1], Ji-Chyun Liu[1], Chee-Ming Eea[1], Ching-Huei Lin[1], Wen-Lung Lu[1], Ching-Tsan Chiang[1], Yung-Sheng Lee[2], and Ada Hui-Chuan Chen[3]

Key words: super typhoons, satellite imagery, cold fronts.

ABSTRACT

This paper presents a framework involving the use of remote sensing imagery and image processing techniques to analyze a 2014 super typhoon, Typhoon Nuri, and the cold occlusion that occurred in the northwestern Pacific Ocean. The purpose of this study was to predict the tracks and profiles of Typhoon Nuri and the corresponding association with the induction of cold front occlusion. Three-dimensional typhoon profiles were implemented to investigate the in-depth distribution of the cloud top from surface cloud images. The results showed that cold fronts and southwesterly airflow accompanied by warm air masses occurred at the front ends of the typhoon during winter, and that cold front occlusion was further intensified by the interactions between these aspects. Over the course of Typhoon Nuri's track, the occluded front grew in length because of its relatively rapid movement, enabling it to pull the edge of the super typhoon. The extension of the occluded front caused the typhoon track to turn and weaken. The occluded fronts were distributed with various lengths of 180-2,880 km and swaths of 40-1,040 km. Temperatures of cloud tops from surface cloud images increased from -55 to -25°C, implying the presence of a typical warm-type occluded front. The cold fronts and southwesterly airflow induced the cold occlusion, revealing a new aspect regarding the occurrence of the cold occlusion associated with typhoon movement and the cause of a decrease in typhoon intensity. A wide variety of weather patterns could be observed along the occluded fronts, with the possibility of thunderstorms and cloudy conditions accompanied by patchy rain or showers.

I. INTRODUCTION

Investigating the effects of climate variability and global warming on the frequency, distribution, and variation of tropical storms (TSs) is valuable for disaster prevention (Gierach and Subrahmanyam, 2007; Acker et al., 2009). Cloud images provided by satellite data can be used to analyze the cloud structures and dynamics of typhoons (Wu, 2001; Pun et al., 2007; Pinẽros et al., 2008, 2011; Liu et al., 2009; Zhang and Wang, 2009). When two tropical cyclones (TCs) are close together, they affect each other by causing rotation. This phenomenon is called "cyclone-cyclone interaction" or the "Fujiwhara effect," named after Fujiwhara, who performed a series of pioneering laboratory experiments on interactions between pairs of vortices in a water tank (1923). Previous studies have discerned several types of cyclone-cyclone interaction (Priẽto, 2003; Joung et al., 2007; Yang et al., 2012). Recently, changes in the separation distance, intensity, and translation speed of binary typhoons have been investigated. The effects of binary typhoons on upper ocean environments were explored, including effects on both physical and biological environments (Yang et al., 2012). Furthermore, in-teractions between medium-strength tropical depressions (TDs) and TCs are a type of cyclone-cyclone interactions. Studying various types of cyclone-cyclone interaction is useful for weather forecasting. For example, a previous study reported that in the North Pacific Ocean a medium-strength TC, Typhoon Bopha (located between Typhoons Saomai and Wukong), had an unusual movement in the western. The researchers quantitatively determined that Typhoon Bopha moved southward due to the circulation associated with Typhoon Saomai; Typhoon Wukong affected the motion of Typhoon Bopha, and the flow field associated with Typhoon Bopha steered Typhoon Soamai (Wu et al., 2003). In one recent case, medium-strength TDs appeared between

Paper submitted 11/01/16; revised 09/09/16; accepted 07/06/17. Author for correspondence: Kuan-Dih Yeh (e-mail:kdyeh@uch.edu.tw).
[1] Dept. of Electrical Engineering, Chien Hsin University of Science and Technology, Chung-li, Tao-yuan, Taiwan, R.O.C.
[2] Dept. of Computer Science and Information Engineering, Chien Hsin University of Science and Technology, Chung-li, Tao-yuan, Taiwan, R.O.C.
[3] Dept. of Information Management, Chien Hsin University of Science and Technology, Chung-li, Tao-yuan, Taiwan, R.O.C.

Typhoons Tembin and Bolaven, which were located far from each other. Because the TDs were smaller and lower than the TCs, an upward convection occurred between the TCs and TDs in addition to attraction. Individual interactions between medium-strength TDs and TCs, called depression-cyclone interactions, caused indirect cyclone-cyclone interactions, despite the distance between the two typhoons being more than 1500 km (Liu et al., 2015). In another study, the response of the sea surface temperature before and after the passage of Typhoon Songda was investigated using satellite infrared cloud images and a three-dimensional (3D) model. Asymmetrical cyclonic surface wind generated by the combination of the movement and cyclonic winds of the typhoon could cause the divergence of wind-driven currents (Choi et al., 2012). In one study, the Regional Ocean Modeling System was used to reproduce the upper ocean response to the passage of Typhoon Sinlaku, and the simulated upper ocean cooling model and the response observed by satellite microwave sensors were presented (Zheng et al., 2015).

Super typhoons, extratropical cyclones, and hurricanes have been studied extensively (Wang et al., 1994; Direk and Chandrasekar, 2006; Jelenak et al., 2009; Walker et al., 2009; Zheng et al., 2009; Miles et al., 2013; Adriano et al., 2014). A close examination of both active and passive microwave signatures conducted at the Hong Kong observatory showed that a significant scattering of radiation at a frequency of 18 GHz occurred in the inner eyewall at altitudes of 3-8 km during a super typhoon (Wang et al., 1994). A classification of the vertical profiles of reflectivity based on Tropical Rainfall Measuring Mission (TRMM) precipitation radar observations obtained using self-organizing maps was presented, with the results showing that hurricanes contain characteristic profiles similar to those of typhoons and with equal or higher reflectivity (Direk and Chandrasekar, 2006). Through analyzing the composite reflectivity, vertical wind shear, and radial velocity of a storm based on Doppler radar observations, some typical properties such as speed shear and mesocyclones were discovered (Zheng et al., 2009). The researchers used the following sources of satellite measurements available in near real time: infrared measurements and nighttime composites of sea surface temperature from Geostationary Operational Environmental Satellite 12, gridded sea surface height maps derived from multiple-satellite altimetry, and microwave sea surface temperature measurements from the TRMM's Microwave Imager and Advanced Microwave Scanning Radiometer for EOS. Accurate predictions of a hurricane's track and intensity can be applied to enhance public safety during hurricane seasons (Walker et al., 2009). QuikSCAT measurements of extratropical cyclones in the North Pacific that reached hurricane force wind strength during seven cold seasons from 2001 to 2008 were used to study these cyclones' average wind speed distribution (Jelenak et al., 2009). The Mid-Atlantic Bight has experienced numerous extratropical cyclones and hurricanes in recent years that have caused extensive damage along coastlines. Understanding coastal oceans ahead of such events is critical for accurately forecasting storm intensity (Miles et al., 2013). The extent of flooding in the Philippines caused by a super typhoon, Typhoon Haiyan, was determined using images from the Advanced Spaceborne Thermal Emission and Reflection Visible Near Infrared telescope. The phase-based analysis was verified using damage levels obtained through visual damage inspection of high-resolution satellite images (Adriano et al., 2014).

In one study, typhoon features were investigated and an analysis of various typhoon images was presented. Recently, an objective technique has been developed to automatically locate the center of a TC by using satellite-generated infrared (IR) images. Observations were recorded at 30-min intervals in three channels: the visible channel (0.55-0.75 μm), water vapor absorption channel (5.6-7.2 μm), and thermal IR window channel (10.5-12.5 μm). The objective was to determine the point around which the fluxes of the gradient vectors of the brightness temperature converge (Jaiswal and Kishtawal, 2013). The spectral features of geostationary satellite IR window channel and water vapor channel data were used to calculate parameters to determine the overshooting areas in typhoon cloud systems and the centers and intensities of typhoons. The satellite data were used to provide hourly observations of visible data from two IR channels, namely IR1 (10.5-11.5 μm) and IR2 (11.5-12.5 μm), and a water vapor channel (6.5-7.0 μm) (Liu et al., 2015). Because ice clouds and ice-covered surfaces on clouds have been observed using shortwave IR (SIR) channels (King et al., 2003; Plantnick et al., 2003; Huang et al., 2004; Hong et al., 2007; Minnis et al., 2011a, 2011b), and based on cloud effective temperatures and optical depths with 3.7-μm (Plantnick et al., 2003) or 3.8-μm (Minnis et al., 2011a) detectors, the researchers utilized a variety of empirical methods to crudely characterize the vertical structures of clouds (Minnis et al., 2011a). The present study also applied an SIR channel with 3.7 μm to detect cloud images of typhoons to observe the cloud surfaces in depth.

In the Hong Kong observatory, the classification of TCs is defined in terms of wind speeds averaged over 10-min periods. A super typhoon is defined as having wind speeds of 185 km/h (pressure of 926 hPa) or higher. The recent increase in global climate variability caused many super typhoons in the northwestern Pacific Ocean in 2014. The Hong Kong observatory reported that approximately eight super typhoons occurred, seven of which affected East Asian countries such as the Philippines, China, Taiwan, South Korea, and Japan. The present study analyzed a super typhoon, Typhoon Nuri, that occurred on November 03, 2014 (910 hPa) and its surrounding environments including cold fronts and southwesterly air flow. A cold front is the leading edge of a cool air mass that exerts a greater temperature gradient between itself and the typhoon's circulation. A southwesterly airflow is a type of warm front. The intensity of a typhoon is partially controlled by cold fronts and southwesterly airflow. In summer, southwesterly airflow usually has the potential to increase the intensity of super typhoons. In winter, cold fronts and southwesterly airflow have the potential to increase or decrease typhoon intensity. This paper presents case studies of Typhoon Nuri to enhance the understanding of cold fronts and southwesterly airflow and their interaction with Typhoon Nuri in the winter of 2014.

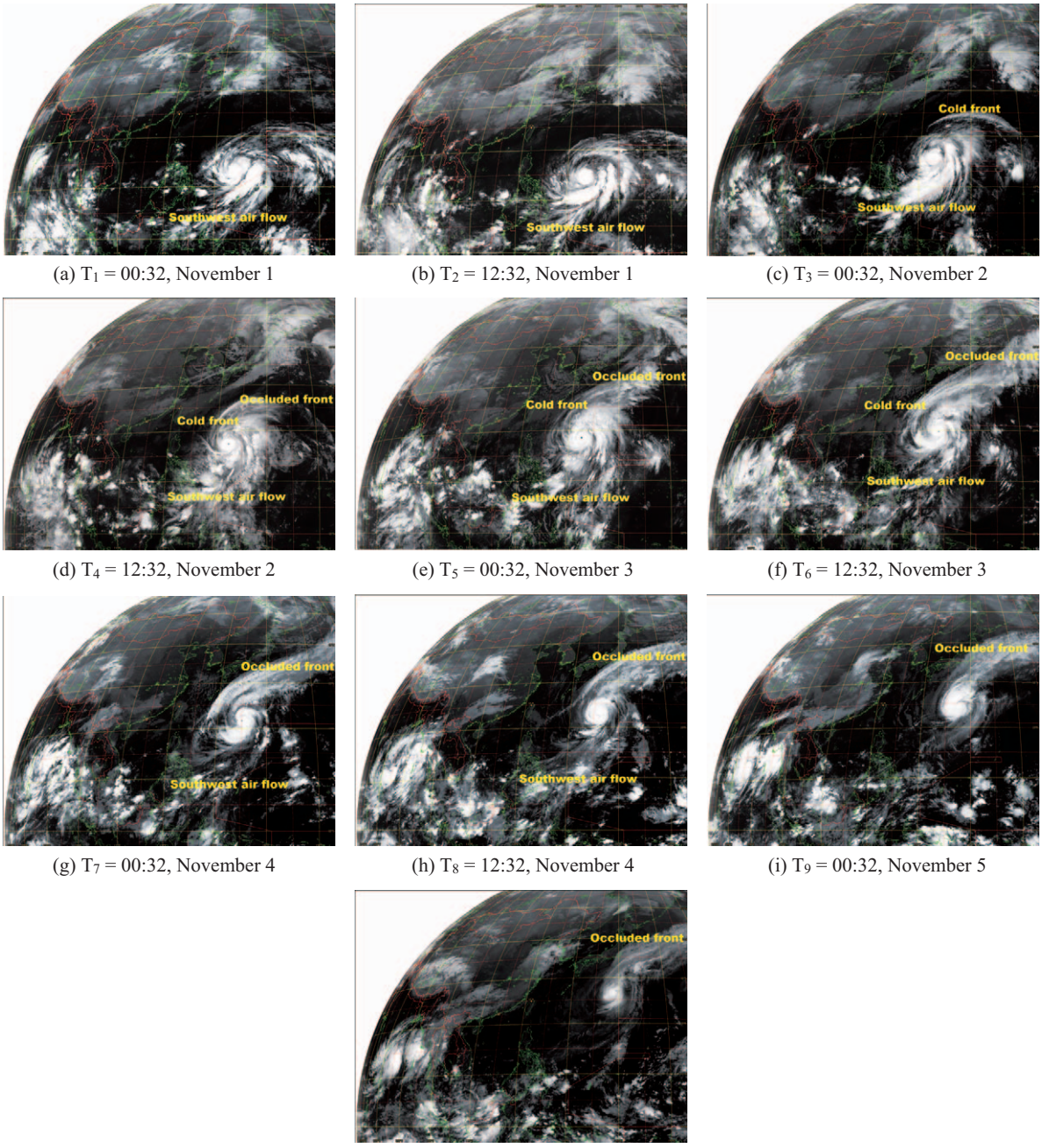

(a) T_1 = 00:32, November 1
(b) T_2 = 12:32, November 1
(c) T_3 = 00:32, November 2
(d) T_4 = 12:32, November 2
(e) T_5 = 00:32, November 3
(f) T_6 = 12:32, November 3
(g) T_7 = 00:32, November 4
(h) T_8 = 12:32, November 4
(i) T_9 = 00:32, November 5
(j) T_{10} = 12:32, November 5

Fig. 1. Cloud images of Typhoon Nuri.

Typhoon Nuri was initially classified as a TD when it formed over the western Pacific Ocean and east-southeastern Guam on October 30, 2014. It increased in intensity over the subsequent few days. On November 1, Typhoon Nuri was initially upgraded to a severe TS, and then, under the influence of southwesterly airflow and excellent outflow, intensified into a typhoon when the system was turning northward and forming an eye. The system deepened rapidly on November 2, depicting a round eye embedded in a superdeep convection. Shortly before reaching peak intensity with a round eye late on November 2, Typhoon Nuri was classified as one of seven super typhoons in 2014. After maintaining peak intensity for 1 day, Typhoon Nuri began to gradually weaken on November 4 because of cold occlusions among the neighboring southwesterly airflow and oncoming cold fronts. On November 4, the structure of Typhoon Nuri decayed further, and the eye feature was completely lost on November 5. Because of the occluded fronts, Typhoon Nuri became partially exposed and accelerated northeastward on November 5, causing landfall over Japan. The storm shifted directly east of Japan and gradually weakened after November 6.

When a warm air mass encounters a cold air mass, a cold occlusion occurs if a cold front lifts a warm front. Typically, three types of atmospheric fronts are generated: a warm front, cold front, and occluded front. A wide variety of weather patterns can be found along occluded fronts, with thunderstorms also possible. This can result in the three air masses being piled on top of one another. When moisture is in place, heavy precipitation and storms can occur. Nevertheless, over time, the occluded front grows in length because of its relatively fast movement, and it draws the center of the low pressure away from the heat and moisture, typically causing the TC to weaken. Recently, surface imprints of atmospheric occluded fronts were revealed by synthetic aperture radar images. Consequently, the occluded front was characterized as a low-wind zone located between two zones of higher winds blowing in opposite directions to the left and right sides of the occluded front (Li et al., 2015).

In the northwestern Pacific Ocean, a cold front exerts a temperature gradient in the northern part of a typhoon, and southwesterly winds convey warm and humid air to the southern part of the typhoon, thereby affecting the typhoon's intensity. Therefore, except for the higher quality visualization of the intensity variety among cold fronts, southwesterly airflow, and typhoons, a 3D profile was employed in this study to provide more information on satellite images. The case study of Typhoon Nuri was conducted to enhance the understanding of cold fronts and southwesterly airflow and their interaction with Typhoon Nuri in the winter of 2014. The intensity variety and size among cold fronts, southwesterly airflow, and typhoons were used to expound cold front–southwesterly airflow interaction, the induction of cold occlusion, and the reduction in typhoon coverage that causes typhoons to turn and weaken. Finally, typhoon cloud images, tracks, 3D profiles, centers, and occluded fronts were all used in the present analysis. Further observation and quantification of interactions could facilitate weather prediction models and forecasts.

II. SATELLITE CLOUD IMAGES OF TYPHOON NURI (2014)

To investigate the distributions of Typhoon Nuri, we analyzed satellite cloud images of Nuri from 2014. Using multifunctional transport satellite (MTSAT) IR cloud images, we implemented 3D typhoon profiles to investigate the in-depth distribution of the cloud top from a surface cloud image (Liu et al., 2015). Figs. 1(a)-(j) show cloud images of Typhoon Nuri at the following times: (a) T_1 = 00:32, November 1; (b) T_2 = 12:32, November 1; (c) T_3 = 00:32, November 2; (d) T_4 = 12:32, November 2; (e) T_5 = 00:32, November 3; (f) T_6 = 12:32, November 3; (g) T_7 = 00:32, November 4; (h) T_8 = 12:32, November 4; (i) T_9 = 00:32, November 5; and (j) T_{10} = 12:32, November 5.

Figs. 1(a) and (c) evidently show that the southwesterly airflow under Typhoon Nuri at T_1, T_2, and T_3 shifted from a northwesterly direction. Typhoon Nuri was enhanced by the southwesterly airflow and became stronger during T_4-T_7. Typhoon

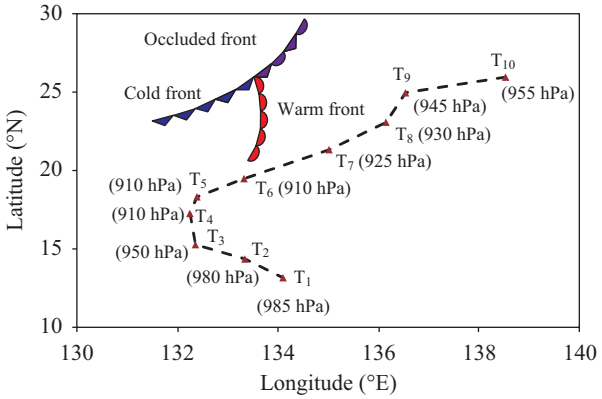

Fig. 2. Tracks of Typhoon Nuri (2014).

Nuri could be detected by inspecting its eye sizes. The cold front moved close to Typhoon Nuri in T_3 and T_4, and the occlusion of the front began at T_4 (Figs. 1(c) and (d)). Subsequently, the occluded fronts grew up and formed another air mass during T_5-T_8 (Figs. 1(e)-(h)). During T_8-T_{10}, the intensity of Typhoon Nuri decreased (Figs. 1(h)-(j)). Typhoon Nuri shifted northward during T_4-T_7, and its direction shifted northeastward after T_7.

The tracks of Typhoon Nuri are plotted in Fig. 2. The typhoon formed at the turning point of its track and was located at 17°25'N (latitude) and 132°24'E (longitude). The inclination angles of the typhoon track were from 35° to 90°. Its lowest central pressure of 910 hPa was observed at 17°25'N and 132°24'E atT_4, 18°31'N and 132°38'E atT_5, and 19°48'N and 133°32'E at T_6. During T_1-T_{10}, Typhoon Nuri shifted 1,920 km, and under low central pressure inducing high wind speeds, its intensification caused wind speeds to become strong and violent.

The in-depth temperature distributions of the cloud top in surface cloud images depicted the vertical variation of Typhoon Nuri. The 3D profiles of Typhoon Nuri were constructed from two dimensional (2D) cloud images and the super typhoon's vertical variations. For rectangular coordinates (x, y, h), the projective cloud image is presented on the x-y plane, and the temperature of the cloud top is presented with the height along the h axis. The scales of 2D cloud images on the x-y plane are presented in km. The vertical scales of the cloud top on the *h* axis are represented by temperatures (°C) from -77 to 20°C, with -77°C being the highest temperature (white) on the surface of the cloud top and 20°C being the temperature (dark) on the seawater surface. Because the cold occlusion occurred at T_4 and the super typhoon existed during T_4-T_6, the 3D typhoon profiles and occluded fronts were constructed during T_4-T_6. The 3D profile of Typhoon Nuri at T_5 is shown in Fig. 3. Because the IR detectors were saturated at -77°C, these represent the highest intensities of the super typhoon, with the white area representing the saturated area. The contour map of Typhoon Nuri at T_5 is presented in Fig. 4, indicating that it is similar to the landform feature of the topographic map where the eye is expressed at the center (red) and the eyewall is presented with the decrement contours (blue). The modified 3D profile is shown in Fig. 5.

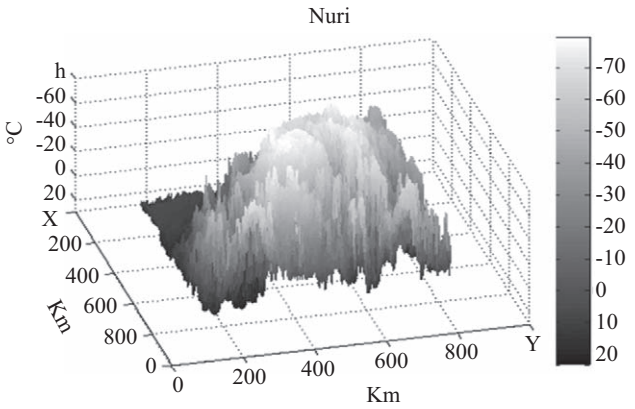

Fig. 3. 3D profile of Typhoon Nuri and occluded front at T_5 = 00:32, November 3.

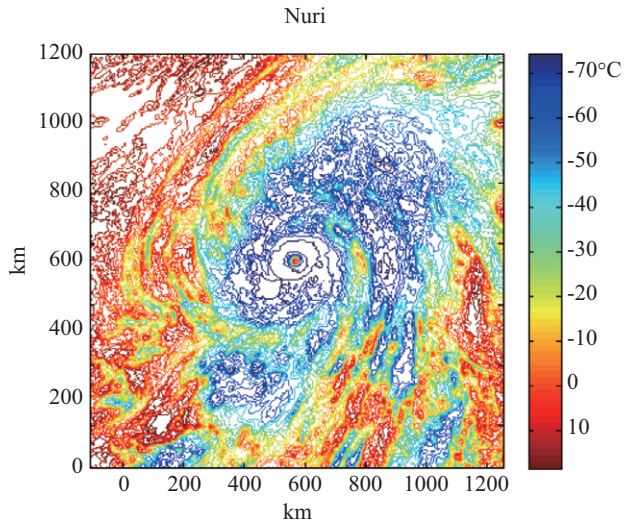

Fig. 4. Contour map of Typhoon Nuri and occluded front at T_5 = 00:32, November 3.

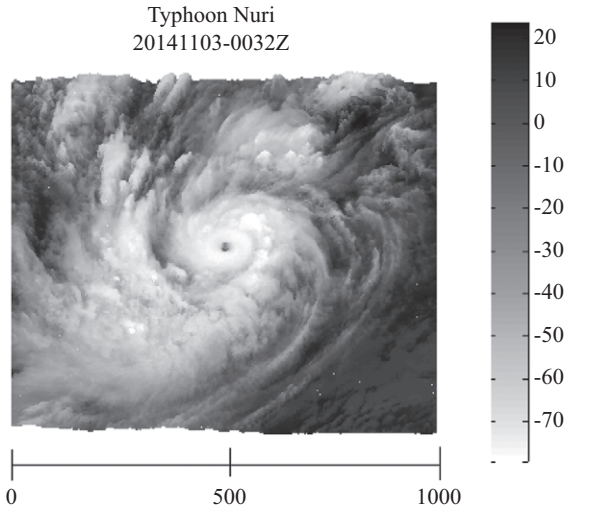

Fig. 5. Modified 3D profile of Typhoon Nuri and occluded front at T_5 = 00:32, November 3.

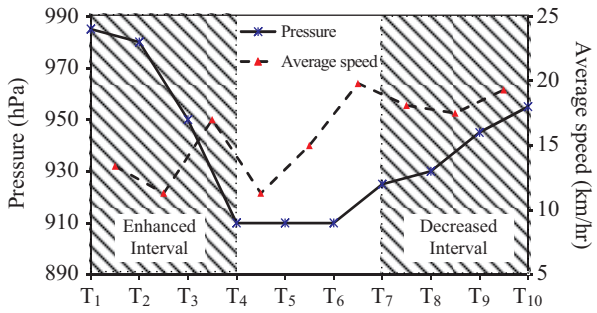

Fig. 6. Time series of pressure versus average speed for Typhoon Nuri during T_1-T_{10}.

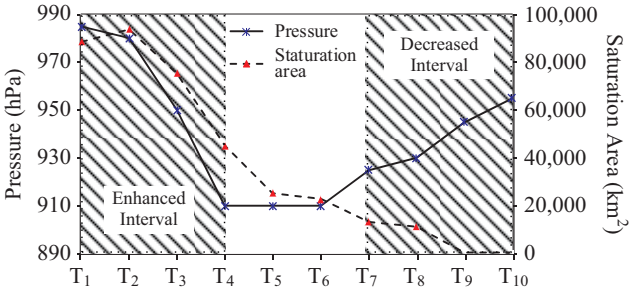

Fig. 7. Time series of pressure versus saturation area observed for Typhoon Nuri during T_1-T_{10}.

III. DISCUSSION AND ANALYSIS

The performance of this study on a super typhoon is discussed in terms of pressures, average speeds of typhoon movements, saturation areas, cloud top temperatures of occluded fronts, lengths and swaths of occluded fronts, and temperature differences in funnels and eye diameters. The temperature differences in the funnels were detected from the tops of the funnels to the centers of the eyes. The parameters of average speeds and saturation areas related to pressure are analyzed in Figs. 6 and 7. Fig. 6 presents the time series of pressure versus average speed for Typhoon Nuri during T_1-T_{10}. As the pressure gradually decreased from 985 (T_1) to 910 (T_4) hPa, the southwesterly air flow was enhanced during T_1-T_4. For the super typhoon intervals, the lowest central pressure value (910 hPa) was presented during T_4-T_6. Typhoon Nuri decreased because of the occluded fronts, and the pressure increased slowly to 955 hPa (T_{10}) during the decreased period of T_7-T_{10}. Except for the higher average speed of 17.0 km/h during T_3 and T_4, lower average speeds of 13.4, 11.3, and 11.3 km/h occurred during T_1-T_2, T_2-T_3, and T_4-T_5, respectively, and increased average speeds of 15.0, 19.8, 18.1, 17.5, and 19.3 km/h occurred during T_5-T_{10}.

The time series of pressure versus saturation area for Typhoon Nuri during T_1-T_{10} are presented in Fig. 7. The larger saturation areas of Typhoon Nuri were 75,500-94,000 km^2 during T_1-T_3 after the enhancement of the southwesterly airflow. As the cold fronts approached, the occluded fronts reduced the saturation

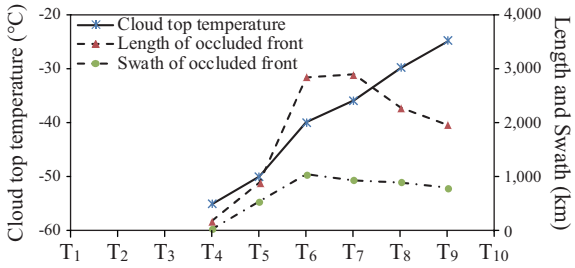

Fig. 8. Time series of cloud top temperature versus length and swath observed for occluded fronts during T_1-T_{10}.

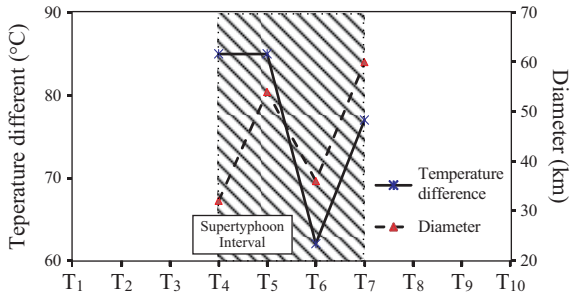

Fig. 9. Time series of temperature difference in funnels versus eye diameter observed for Typhoon Nuri during T_1-T_{10}.

areas of Typhoon Nuri from 45,200 to 13,300 km^2 during T_4-T_7. Finally, the saturation areas decreased from 11,300 to 300 km^2 during T_8-T_{10} because of the occluded fronts.

The time series of the cloud top temperatures and the lengths and swaths of the occluded fronts during T_4-T_{10} are shown in Fig. 8. Because of the occluded fronts with warm southwesterly airflow formed by the interaction between the southwesterly airflow and cold front, the cloud top temperatures of the occluded fronts increased from -55 to -25°C during T_4-T_{10}, indicating the presence of a typical warm-type occluded front. The lengths and swaths of the occluded fronts increased from 180 to 2,880 km and from 40 to 1,040 km, and other new air masses due to the occluded fronts were observed.

Fig. 9 shows the time series for the temperature variations among the funnels and eye diameters for Typhoon Nuri during T_4-T_7. Temperature variations among funnels represent funnel depths. The lack of temperature differences at T_1 implied that no funnels or eyes were present at this time. The temperature difference in the funnels was 85°C at T_4. The temperature differences in the funnels were 85-62°C during T_4-T_7, implying that the funnel was deep and that the super typhoon was formed through the enhancement of the southwesterly airflow. The temperature differences that occurred during T_8-T_{10} decreased and disappeared because of the effects of the occluded fronts. For the super typhoon intervals, the eye diameters were 32-60 km during T_3-T_7. Clear whole eyes could be observed.

In accordance with the results of a previous study (Fig. 1(b), Fig. 8(d), Fig. 9(d), and Fig. 10(d)) (Bai and Wei, 2011), a cloud mountain (3D surface) was constructed using pixels within cloud bands, leading to a mountain terrain assuming the form of a helix. The spiral pattern was extracted using the mountain-climbing algorithm. In the present study, we investigated how "the in-depth temperature distributions of the cloud top from surface cloud images present vertical variations of typhoons. The 3D profiles of the super typhoon were constructed from 2D cloud images and vertical variations of the typhoon." This method is consistent with that of one the previous study (Bai and Wei, 2011).

IV. CONCLUSIONS

In this study, remote sensing imagery and image processing techniques were used to analyze Typhoon Nuri and the cold occlusion that occurred in the northwestern Pacific Ocean. Our overall goal was to assess the potential role that satellite cloud images play in improving the forecasting of super typhoons. Typhoons regularly occur during summer, and southwesterly airflow usually has the potential to increase the intensity of a super typhoon. However, because of the effects of climate variability and global warming in recent years, super typhoons may now frequently occur in winter. In such events, the intensity of typhoons is partially controlled by cold fronts and southwesterly airflow.

Both cold fronts and southwesterly airflow have the potential to increase or decrease super typhoon intensity in winter. This study focused on investigating the extent to which southwesterly airflow and occluded fronts influence changes in typhoon intensity, such as the enhancement or reduction of the intensity during the super typhoon's passage. We analyzed images of Typhoon Nuri inform the winter of 2014. The proposed 3D typhoon profiles are available for investigating the in-depth distribution and the track of a typhoon. The versatile 3D profiles of satellite cloud images could improve typhoon forecasting.

The performance of this research is discussed in terms of pressure, average speeds of typhoon movements, saturation areas, cloud top temperatures of occluded fronts, lengths and swaths of occluded fronts, and temperature differences in funnels and eye diameters, all of which were available for analysis. The temperature differences in the funnels were detected from the tops of the funnels to the centers of the eyes, and the distributions were applied to investigate the in-depth distribution of the funnels. Central pressures and saturation areas indicate wind speed and typhoon intensity.

The results show that cold fronts and southwesterly airflow occasionally occurred at the front of the typhoon, and that both fronts interacted with each other in the winter, resulting in the induction of cold occlusion. Occluded fronts formed during cold occlusions. The occluded front grew in length because of its relatively rapid movement. As the occluded front pulled the edge of the typhoon, it caused the typhoon track to turn and weaken. The occluded fronts distributed with the varied lengths of 180-2,880 km and swaths of 40-1,040 km. These aspects yielded strong airflow with high levels of vapor. As the temperatures of the cloud tops from the surface cloud images increased from -55 to -25°C, the occluded front should have been a typical

warm-type front.

As the central pressure of the super typhoon gradually decreased from 985 (T_1) to 910 (T_4) hPa, it was enhanced by the southwesterly airflow during the enhanced interval T_1-T_4. For the super typhoon intervals, the lowest pressure level (910 hPa) occurred during T_4-T_6. Subsequently, Typhoon Nuri was reduced by the occluded fronts, and the pressure slowly increased to 955 hPa (T_{10}) during the decreased interval of T_7-T_{10}. Except for the higher average speed of 17.0 km/h during T_3 and T_4, lower average speeds of 13.4, 11.3, and 11.3 km/h occurred during T_1-T_2, T_2-T_3, and T_4-T_5, respectively, and increased average speeds of 15.0, 19.8, 18.1, 17.5, and 19.3 km/h occurred during T_5-T_{10}. The average speeds related to the pressure were consistent.

The larger saturation areas of Typhoon Nuri were 75,500-94,000 km^2 during T_1-T_3 after the enhancement of southwesterly airflow. As the cold fronts approached, the occluded fronts engendered the reduction of the saturation areas of Typhoon Nuri from 45,200 to 13,300 km^2 during T_4-T_7. Finally, the saturation areas decreased from 11,300 to 300 km^2 during T_8-T_{10} because of the occluded fronts. The saturation areas of the cloud images illustrate various intensities of the super typhoon.

The temperature differences in funnels represent their depth. In this study, the lack of a temperature difference at T_1 implies the lack of a funnel or eye at this time. The temperature differences in the funnels were 85°C at T_4 and 85-62°C during T_4-T_7, implying that the deep depth of the funnel and the super typhoon were results of the enhancement of the southwesterly airflow. The temperature differences at T_8 and T_{10} decreased and disappeared because of the effects of the occluded fronts. For the super typhoon intervals, the eye diameters were 32-60 km during T_3-T_7. The whole eyes were clearly observable.

Cold fronts and southwesterly airflow represent the cold occlusion that influences the typhoon's movement and decreases the intensity of the typhoon. Occluded fronts bring the potential for a wide variety of weather patterns, with the possibility of thunderstorms, creating cloudy conditions with patchy rain or showers. Further improvement in techniques to quantitatively observe and explain the interaction between cold fronts and southwesterly airflow and typhoons could facilitate more effective weather forecasting.

ACKNOWLEDGMENTS

We gratefully acknowledge Professor Liou Y. A. of the Center for Space and Remote Sensing Research at National Central University, Taiwan.

REFERENCES

Acker J., P. Lyon, F. Hoge, S. Shen, M. Roffer and G. Gawlikowski (2009). Interaction of Hurricane Katrina with optically complex water in the Gulf of Mexico: Interpretation using satellite-derived inherent optical properties and chlorophyll concentration. IEEE Geoscience and Remote Sensing Letters 6(2), 209-213.

Adriano, B., H. Gokon, E. Mas, S. Koshimura, W. Liu and M. Matsuoka (2014). Extraction of damaged areas due to the 2013 Haiyan typhoon using ASTER data. IEEE Geoscience and Remote Sensing Symposium 2154-2157.

Bai, Q. and K. Wei (2011). Cloud system extraction in tropical cyclones by mountain-climbing. Atmospheric Research 101, 611-620.

Choi H., M. S. Lee and S. M. Choi (2012). Cold sea surface temperature near Cheju island responding to strong cyclonic wind and positive geopotential tendency behind a typhoon center along its track, Journal of Marine Science and Technology 20(6), 684-692.

Direk K. and V. Chandrasekar (2006). Study of hurricanes and typhoons from TRMM precipitation radar observations: Self organizing map (SOM) neural network. IEEE Geoscience and Remote Sensing Symposium 45-48.

Fujiwhara S. (1923). On the growth and decay of vortical systems. Quarterly Journal of the Royal Meteorological Society 49, 75-104.

Gierach M. M. and B. Subrahmanyan (2007). Satellite data analysis of the upper ocean response to hurricanes Katrina and Rita (2005) in the Gulf of Mexico. IEEE Geoscience and Remote Sensing Letters 4(1), 132-136.

Huang H. L., P. Yang, H. Wei, B. A. Baum, Y. Hu, P. Antonelli and S. A. Ackerman (2004). Inference of ice cloud properties from high spectral resolution infrared observations. IEEE Trans on Geoscience and Remote Sensing 42(4), 842-853.

Hong G., P. Yang, H. L. Huang, B. A. Baum, Y. Hu and S. Platnick (2007). The sensitivity of ice cloud optical and microphysical passive satellite retrievals to cloud geometrical thickness. IEEE Trans on Geoscience and Remote Sensing 45(5), 1315-1323.

Jelenak, Z., K. Ahmad, J. Sienkiewicz and P. S.Chang (2009). A statistical study of wind field distribution within extra-tropical cyclones in north Pacific ocean from 7-years of QuikSCAT wind data. IEEE Geoscience and Remote Sensing Symposium I-104-107.

Joung Y. J., M. K. Lin, Y. C. Lin, C. W. Chang and H. H. A. Chen (2007). A simulation of Fujiwhara effect on a structured agent-based peer-to-peer system. Proceedings of the 2007 2nd International Conference on Communication System Software and Middleware and Workshops, 1-7.

Jaiswal N. and C. M. Kishtawal (2013). Objective detection of center of tropical cyclone in remotely sensed infrared images. IEEE Journal of Selected Topics in Applied Earth Observations and Remote Sensing 6(2), 1031-1035.

King M. D., W. P. Menzel, Y. J. Kaufman, D. Tanre, B. C. Gao, S. Plantnick, S. A. Ackerman, L. A. Remer, R. Pincus and P. A. Hubanks (2003). Cloud and aerosol properties, precipitable water, and profiles of temperature and humidity from MODIS. IEEE Trans on Geoscience and Remote Sensing 41(2), 442-458.

L, X., X. Yang, W. Zheng, J. A. Zhang, J. A. Pietrafesa and W. G. Pichel (2015). Synergistic use of satellite observations and numerical weather model to study atmospheric occluded fronts. IEEE Trans. on Geoscience and Remote Sensing 53(9), 5269-5279.

Liu, C. C., T. Y. Shyu, T. H. Lin and C. Y. Liu (2015). Satellite-derived normalized difference convection index for typhoon observations. J. Appl. Remote Sens. 9 (1), 096074.

Liu C., T. Y. Shyu, C. C. Chao and Y. F. Lin (2009). Analysis on typhoon Long Wang intensity changes over the ocean via satellite data. Journal of Marine Science and Technology 17(1), 23-28.

Liu J. C., Y. A. Liou, M. X. Wu, Y. J. Lee, C. H. Cheng, C. P. Kuei and R. M. Hong (2015). Interactions among two tropical depressions and typhoons Tembin and Bolaven (2012) in pacific ocean: Analysis of the depression-cyclone interactions with 3-D reconstruction of satellite cloud images. IEEE Trans on Geoscience and Remote Sensing 53(3), 1394-1402.

Miles, T., S. Glenn, J. Kohut, G. Seroka and Y. Xu (2013). Observations of hurricane sandy from a glider mounted aquadopp profiler. Oceans 1-8.

Minnis P., S. Sun-Mack, D. F. Young, P. W. Heck, D. P. Garber, Y. Chen, D. A. Spangenberg, R. F. Arduini, Q. Z. Trepte, W. L. Jr. Smith, J. K. Ayers, S. C. Gibson, W. F. Miller, V. Chakrapani, Y. Takano, K. N. Liou and Y. Xie (2011). CERES Edition 2 cloud property retrievals using TRMM VIRS and Terra and Aqua MODIS data: Part I: Algorithms. IEEE Trans on Geoscience and Remote Sensing 49(11), 4374-4400.

Minnis P., S. Sun-Mack, Y. Chen, M. M. Khaiyer, Y. Yi, J. K. Ayers, R. R. Brown, X. Dong, S. C. Gibson, P. W. Heck, B. Lin, M. L. Nordeen, L. Nguyen, R. Palikonda, W. L. Jr. Smith, D. A. Spangenberg, Q. Z. Trepte and B. Xi

(2011). CERES Edition-2 cloud property retrievals using TRMM VIRS and Terra and Aqua MODIS Data-Part II: Examples of average results and comparisons with other data. IEEE Trans on Geoscience and Remote Sensing 49(11), 4401-4430.

Piñeros M. F., E.A. Ritchie and J. S. Tyo (2008). Objective measures of tropical cyclone structure and intensity change from remotely sensed infrared image data. IEEE Trans on Geoscience and Remote Sensing 46(11), 3574-3580.

Piñeros M. F., E.A. Ritchie and J. S. Tyo (2011). Estimating tropical cyclone intensity from infrared image data. Weather and Forecasting 26, 690-698.

Priêto R., B. D. Mcnoldy, S. R. Fulton and W. A. Schubert (2003). A classification of binary tropical cyclone-like vortex interactions. Monthly Weather Review 131, 2656-2666.

Pun I. F., I. I. Lin, C. R. Wu, D. S. Ko and W. T. Liu (2007). Validation and application of altimetry- derived upper ocean thermal structure in the western north Pacific ocean for typhoon-intensity forecast. IEEE Trans on Geoscience and Remote Sensing 45(6), 1616-1630.

Plantnick S., M. D. King, S. A. Ackerman, W. P. Menzel, B. A. Baum, J. C. Riedi and R. A. Frey (2003). The MODIS cloud products: Algorithms and examples from Terra. IEEE Trans on Geoscience and Remote Sensing 41(2), 459-473.

Walker, N., R. Leben, S. Anderson, A. Haag, C. Pilley and M. Korobkin (2009). Exploration of real-time satellite measurements to advance hurricane intensity prediction in the Northern Gulf of Mexico. Oceans 1-9.

Wang, J. R., R. Meneghini, H. Kumagai, T. T. Wilheit, W. C. Jr. Boncyk, P. Racette, J. R. Tesmer and B. Maves (1994). Airborne active and passive microwave observations of super typhoon Flo. IEEE Trans. on Geoscience and Remote Sensing 32 (2), 231-242.

Wu C. C. (2001). Numerical simulation of typhoon Gladys (1994) and its interaction with Taiwan terrain using the GFDL hurricane model. Monthly Weather Review 129, 1533-1549.

Wu C. C., T. S. Huang, W. P. Huang and K. H. Chou (2003). A new look at the binary interaction: Potential vorticity diagnosis of the unusual southward movement of Typhoon Bopha (2000) and its interaction with Typhoon Saomai (2000). Monthly Weather Review 131, 1289-1300.

Yang, Y. J., L. Sun, A. M. Duan, Y. B. Li, Y. F. Fu, Y. F. Yan, Z. Q. Wang and T. Xian (2012). Impacts of the binary typhoons on upper ocean environments in November 2007. J. Appl. Remote Sens. 6 (1), 063583.

Zhang C. J. and X. D. Wang (2009). Typhoon cloud image enhancement and reducing speckle with genetic algorithm in stationary wavelet domain. IET Image Process 3(4), 200-216.

Zheng, F., L. S. Chen and J. F. Zhong (2009). Analysis of a strong tornado in the outer-region of the super typhoon "Sepat" in 2007. 2009 World Congress on Computer Science and Information Engineering 283-287.

Zheng Z. W., N. J. Kuo, Q. Zheng and G. Gopalakrishnan (2015). Modling of upper ocean heat budget variations in response to the passage of super typhoon Sinlaku (2008) in the western north Pacific. Journal of Marine Science and Technology 23(4), 551-557.